



Cite this: *Green Chem.*, 2016, **18**, 3628

## Efficient utilization of photogenerated electrons and holes for photocatalytic selective organic syntheses in one reaction system using a narrow band gap CdS photocatalyst†

Xiaofeng Ning,<sup>a</sup> Sugang Meng,<sup>\*a</sup> Xianliang Fu,<sup>a</sup> Xiangju Ye<sup>b</sup> and Shifu Chen<sup>\*a,b</sup>

In this study, a nanoparticle structure of CdS with cubic phase (CdS-G) was prepared by a facile solid-state reaction at room temperature for the first time. CdS-G can be used as a highly active photocatalyst for selective oxidation of *p*-methoxybenzyl alcohol (pMBA) to *p*-methoxybenzaldehyde (pMBAD) and reduction of nitrobenzene (NB) to aniline (AL) in a coupled reaction system under green mild reaction conditions through visible light irradiation. Compared with the counterparts prepared by the conventional precipitation method (CdS-P) and hydrothermal method (CdS-H), the photocatalytic performance of CdS-G is greatly improved owing to the unique features of the nanostructure, the high surface area, pore volume, visible light absorption and photoelectric properties. The yield of pMBAD (AL) over CdS-G is about 1.6 (5.2) and 1.9 (20.8) times higher than that over CdS-P and CdS-H, respectively. The CdS-G sample exhibits excellent selectivity and stability because its valence band (VB) and conduction band (CB) positions matched well with the redox potentials of pMBA/pMBAD and NB/AL. Furthermore, the photogenerated holes and electrons can be efficiently and directly reacted with pMBA and NB, respectively. The photocatalytic selective oxidation and reduction reaction is a synergistic reaction *via* producing and consuming protons. The photogenerated holes and electrons could be utilized thoroughly to produce pMBAD and AL, respectively. The molar ratio of pMBA and NB was 3 : 1, and the yield of pMBAD and AL could be successfully achieved at a theoretical ratio of 1 : 1. This work highlights the promising scope for selective organic synthesis in one reaction system under mild conditions using photogenerated electrons and holes directly and simultaneously.

Received 28th February 2016,  
Accepted 17th March 2016

DOI: 10.1039/c6gc00572a

www.rsc.org/greenchem

## 1. Introduction

Photocatalytic organic synthesis has been developed in recent years and attracts particular attention because of its milder and greener reaction conditions, the capability to be driven by solar light, and high selectivity.<sup>1–4</sup> Typical examples of photocatalytic organic synthesis are selective oxidation of aromatic alcohols to aromatic aldehydes<sup>5–8</sup> and selective reduction of nitro-aromatic organics to corresponding amino organics,<sup>9–11</sup> because such aldehydes and amines are important industrial intermediates for the synthesis of important chemicals and pharmaceuticals. Traditional synthesis methods produce large

amounts of waste and result in uncontrollability of product selectivity.<sup>12</sup> For example, toxic and corrosive stoichiometric oxidants such as hypochlorite, chlorine and chromate are often used to synthesize aromatic aldehydes;<sup>13</sup> stoichiometric reductants such as pressurized hydrogen as well as transition metal catalysts are required for selective reduction of nitro-aromatic organics.<sup>14</sup> Therefore, from the point of view of green chemistry, photocatalysis would be a promising approach to drive the oxidation or reduction reactions under mild conditions through irradiation by solar light.

Recently, tremendous efforts have been made to synthesize aldehydes and amines through visible-light-driven photocatalysts. For instance, Zhao's group reported that a coupled system of TEMPO and dye-sensitized TiO<sub>2</sub> could oxidize benzyl alcohol using visible light and oxygen.<sup>15</sup> Wang's group found that mpg-C<sub>3</sub>N<sub>4</sub> could be used as a visible-light-driven photocatalyst for selective oxidation of alcohols.<sup>5</sup> However, the photocatalytic activities are both poor. More recently, Xu's group demonstrated that graphene–semiconductor composites could effectively enhance the photocatalytic activity of

<sup>a</sup>Department of Chemistry, Huaibei Normal University, Anhui Huaibei, 235000, People's Republic of China. E-mail: mengsugang@126.com; Fax: +86-561-3090518; Tel: +86-561-3806611

<sup>b</sup>Department of Chemistry, Anhui Science and Technology University, Anhui Fengyang, 233100, People's Republic of China

†Electronic supplementary information (ESI) available. See DOI: 10.1039/c6gc00572a

semiconductors for selective organic transformations under ambient conditions.<sup>16</sup> Meanwhile, Bi<sub>12</sub>O<sub>17</sub>-Cl<sub>2</sub>,<sup>6</sup> BN-based semiconductor composites<sup>17,18</sup> and metal alloys<sup>19,20</sup> were also explored and exhibited high efficiency for photocatalytic organic synthesis under visible light irradiation. This progress provided valuable knowledge for photocatalytic organic synthesis. However, it is known that photocatalysis is based on the band theory of semiconductors and is driven by photoexcited electron-hole pairs.<sup>21</sup> Photogenerated holes and electrons have strong abilities for oxidation and reduction, respectively. Therefore, pressurized oxygen used as an electron scavenger is used during photocatalysis for the selective oxidation of alcohols,<sup>7,8</sup> while the superoxide radicals produced (formed by reaction of electrons and molecular oxygen) might not participate in the oxidation of alcohols.<sup>6</sup> On the other hand, during photocatalytic selective reduction of nitro-aromatic organics, the photogenerated electrons play a decisive role in driving the photocatalytic reduction of nitro-aromatic compounds, and the oxidizing holes must be trapped by a hole-capturer (such as ammonium formate).<sup>22</sup> In other words, the hole is also wasteful and does not perform its own function.

Recently, in our lab, the selective oxidation of aromatic alcohol *via* photogenerated holes and selective reduction of nitro-aromatic compounds through photogenerated electrons were realized in one reaction system. It is known that photogenerated charge separation, charge migration and recombination are the major factors influencing the efficiency of solar energy conversion over photocatalysts.<sup>23–25</sup> If the selective photo-redox process could be realized in a coupled reaction system, not only will the photogenerated electrons and holes fully perform their own role, but also the separation and transfer efficiency of photogenerated charge carriers will be rapidly boosted. As a result, fine chemicals (aldehydes and amines) could be synthesized simultaneously under milder reaction conditions, and the photocatalytic activity of the semiconductor towards target photo-redox processes would also be improved. For this bold assumption, CdS/g-C<sub>3</sub>N<sub>4</sub> composite has been fabricated by our group and shows photocatalytic activity for selective oxidation of benzyl alcohol to benzaldehyde (yield < 50%) and reduction of nitrobenzene to aniline (yield < 30%) under visible light irradiation.<sup>26</sup> Unfortunately, the yields of the target products are very low and the reaction mechanism has not been clarified in detail.

Herein, to circumvent the aforementioned shortcomings, nanoparticle structured CdS with cubic phase was synthesized by a very simple solid-state method at room temperature. This is the first report of the simple preparation method whereby CdS can be easily obtained by grinding a mixture of solid cadmium source and sulfur source. The as-synthesized CdS exhibits remarkable activity for the selective oxidation of *p*-methoxybenzyl alcohol to *p*-methoxybenzaldehyde and reduction of nitrobenzene to aniline in one reaction system under visible light irradiation compared with the reported CdS/g-C<sub>3</sub>N<sub>4</sub> composite and two reference CdS samples synthesized by the conventional hydrothermal process<sup>10</sup> and the precipitation method.<sup>27</sup> This is attributed to its well-

matched conduction band and valence band positions, high surface area, and highly effective separation of photogenerated charge carriers. Furthermore, because the holes and electrons photogenerated from nanoparticle structured CdS react effectively with aromatic alcohol and nitrobenzene, respectively, the photocorrosion of CdS can be prevented effectively. Consequently, CdS is able to show excellent recycling photocatalytic activities towards selective photogenerated hole-driven oxidation and electron-driven reduction processes in a coupled reaction system. Finally, a possible reaction mechanism for this photocatalytic reaction system was proposed based on the results of active species analysis and reaction intermediate detection, and the yield ratio of the target products could successfully achieve theoretical values by controlling the reaction conditions. It is hoped that our work could open new horizons for making best use of photogenerated electron-hole pairs in selective organic transformations.

## 2. Experimental

### 2.1. Materials

Cadmium nitrate (Cd(NO<sub>3</sub>)<sub>2</sub>·4H<sub>2</sub>O, 99%), cadmium acetate dihydrate (Cd(CH<sub>3</sub>COO)<sub>2</sub>·2H<sub>2</sub>O, 99.99%), sodium sulfide (Na<sub>2</sub>S·9H<sub>2</sub>O, 98.0%), thiourea (NH<sub>2</sub>CSNH<sub>2</sub>, 99.0%), benzotrifluoride (C<sub>6</sub>H<sub>5</sub>CF<sub>3</sub>, BTF, 99.0%), benzyl alcohol (C<sub>6</sub>H<sub>5</sub>CH<sub>2</sub>OH, ≥99.0%), *p*-methoxybenzyl alcohol (C<sub>6</sub>H<sub>5</sub>OCH<sub>2</sub>CH<sub>2</sub>OH, pMBA, 98.0%), nitrobenzene (C<sub>6</sub>H<sub>5</sub>NO<sub>2</sub>, NB, 99.0%), *p*-chloronitrobenzene (C<sub>6</sub>H<sub>4</sub>ClNO<sub>2</sub>, 98.0%), phenol (C<sub>6</sub>H<sub>5</sub>OH, 98.0%), triethanolamine (C<sub>6</sub>H<sub>15</sub>NO<sub>3</sub>, 98.0%), tetrachloromethane (CCl<sub>4</sub>, 99.5%), acetonitrile (CH<sub>3</sub>CN, 99%), lithium perchlorate (LiClO<sub>4</sub>, 99.9%), potassium ferricyanide (K<sub>3</sub>Fe(CN)<sub>6</sub>, ≥99.5%), potassium ferrocyanide trihydrate (K<sub>4</sub>Fe(CN)<sub>6</sub>·3H<sub>2</sub>O, 99.0%), potassium chloride (KCl, 99.5%) and anhydrous sodium sulfate (Na<sub>2</sub>SO<sub>4</sub>, 99.0%) were purchased from Aladdin Industrial Inc. All of the reagents were used in the experiments directly. Deionized water used in the synthesis was from local sources.

### 2.2. Preparation of samples

The CdS samples were synthesized by a very simple solid-state reaction method at room temperature. This method guaranteed easy repetition of catalyst preparation. Typically, 1.067 g Cd(NO<sub>3</sub>)<sub>2</sub>·4H<sub>2</sub>O and 1.662 g Na<sub>2</sub>S·9H<sub>2</sub>O were added to an agate jar (addition of excess amounts of Na<sub>2</sub>S·9H<sub>2</sub>O was to ensure complete reaction of Cd<sup>2+</sup>). The mixed reagents were ground for 30 min at 200 rpm, then the products were washed several times with deionized water and fully dried at 353 K in an oven. The obtained CdS sample is denoted as CdS-G.

For the sake of comparison, another two reference CdS samples were also prepared by different methods. According to the reported methods, one reference sample was prepared by the precipitation method.<sup>27</sup> Typically, Cd(CH<sub>3</sub>COO)<sub>2</sub>·2H<sub>2</sub>O was dissolved in 200 mL of deionized water (denoted as solution A, concentration 5 mM) with vigorous stirring. Na<sub>2</sub>S·9H<sub>2</sub>O was dissolved in 200 mL of deionized water (denoted as solution B,

concentration 6 mM). Then, solution B was slowly added dropwise into solution A over 4 h, and was aged for 36 h with vigorous stirring. The products were washed several times with water, and fully dried to obtain the final product, namely CdS-P. Another reference CdS sample was obtained through a facile hydrothermal treatment.<sup>10</sup> In a typical synthesis, 3.2 mmol of  $\text{Cd}(\text{CH}_3\text{COO})_2 \cdot 2\text{H}_2\text{O}$  and 16 mmol of  $\text{NH}_2\text{CSNH}_2$  were dissolved in 40 mL of deionized water to form a clear solution after stirring for 30 min at room temperature. Subsequently, the solution was transferred into a Teflon-lined stainless steel autoclave with 50 mL capacity and maintained at 140 °C for 24 h. The orange red precipitate was washed several times with deionized water to remove possible remaining cations and anions before being fully dried at 353 K in an oven; this product was denoted as CdS-H.

### 2.3. Characterization

The crystal phase properties of the samples were analyzed with a Bruker D8 Advance X-ray diffractometer (XRD) using Cu K $\alpha$  radiation at 40 kV and 40 mA in the  $2\theta$  range from 15° to 80° with a scan rate of 3° min<sup>-1</sup>. Scanning electron microscopy (SEM) images were obtained by a field emission SEM on a FEI Nova NANOSEM 230 spectrophotometer. Transmission electron microscopy (TEM) images and high-resolution transmission electron microscopy (HR-TEM) images were collected on a JEOL model JEM 2100 EX instrument at an accelerating voltage of 200 kV. The optical properties of the samples were analyzed by UV-Vis diffuse reflectance spectroscopy (UV-Vis DRS) using a UV-Vis spectrophotometer (Cary-500, Varian Co) with BaSO<sub>4</sub> as a reflectance standard. Photoluminescence (PL) emission spectra were recorded on a JASCO FP-6500 type fluorescence spectrophotometer with an excitation wavelength of 440 nm light at room temperature. The Brunauer-Emmett-Teller (BET) specific surface area ( $S_{\text{BET}}$ ) of the samples was analyzed by nitrogen adsorption-desorption in a Micromeritics ASAP 2020 apparatus. To obtain the surface composition of the samples, X-ray photoelectron spectroscopy (XPS) measurement was performed on a Thermo Scientific ESCA LAB 250 photoelectron spectrometer which consisted of a monochromatic Al K $\alpha$  ray beam (1486.6 eV) as the X-ray source, a hemispherical analyzer, and a sample stage with multiaxial adjustability. All of the binding energies were corrected with reference to the C 1s peak of the surface adventitious carbon at 284.6 eV.

### 2.4. Photoelectrochemical performance

All of electrochemical experiments were performed with a CHI-660E electrochemical workstation (CHI Instruments, USA). The photocurrent and electrochemical impedance spectroscopy (EIS) were detected using a conventional three-electrode cell, with an as-prepared CdS electrode (50 mm × 50 mm, ITO/CdS) as working electrode, a Pt wire as the counter electrode, and an Ag/AgCl electrode as reference electrode. The visible light source was a 300 W Xe arc lamp (PLS-SXE 300, Beijing Perfect light Co. Ltd) system equipped with a UV-CUT filter ( $\lambda > 420$  nm). The Mott-Schottky (M-S)

experiments were conducted to evaluate the band positions of the as-prepared samples. According to theoretical calculations for CdS, the potential range was chosen between -1.0 and +0.5 V with potential steps of 0.001 V with different frequencies. The electrolyte was 0.1 mol L<sup>-1</sup> LiClO<sub>4</sub> acetonitrile solution. Cyclic voltammetry (CV) was measured by sweeping at 0.05 V s<sup>-1</sup> in CH<sub>3</sub>CN/0.1 mol L<sup>-1</sup> LiClO<sub>4</sub>/(0.1, 0.2 and 0.5 mmol L<sup>-1</sup>) X (X was pMBA, pMBAD or NB) solution. A glass carbon disk, a platinum wire and an Ag/AgCl electrode were used as the working, counter and reference electrodes, respectively. The redox potentials of pMBA, pMBAD and NB were evaluated from the results of voltammogram analysis.

### 2.5. Evaluation of photocatalytic activity

Photocatalytic selective oxidation of aromatic alcohols to corresponding aromatic aldehydes and reduction of nitrobenzene to aniline were performed as follows: a mixture of aromatic alcohol ( $2.55 \times 10^{-2}$  mol L<sup>-1</sup>), nitrobenzene ( $8.5 \times 10^{-3}$  mol L<sup>-1</sup>), and 0.1 g catalyst were dispersed in benzotrifluoride (BTF, 15 mL). The above mixture was placed in a self-designed photochemical 100 mL reactor, which was filled with molecular nitrogen at a pressure of 0.1 MPa, and stirred for 30 min in the dark to ensure the equilibrium of adsorption-desorption between the photocatalyst and the reactants before irradiation. The suspension was irradiated by a 300 W Xe arc lamp with a UV-CUT filter to cut off light of wavelength <420 nm. Due to continuous cooling with refrigerated circulating water, the temperature of the reaction solution could be maintained at approximately 50 °C. After illumination reaction, the mixture was centrifuged to completely remove the catalyst particles. The remaining solution was analyzed by gas chromatography (Fuli 9790, China) with FID detector. Conversion, yield and selectivity for selective oxidation of alcohols to target product and reduction of nitro-aromatic organics to target product were defined as follows:

$$\text{Conversion (\%)} = [(C_0 - C_r)/C_0] \times 100$$

$$\text{Yield (\%)} = C_p/C_0 \times 100$$

$$\text{Selectivity (\%)} = [C_p/(C_0 - C_r)] \times 100$$

where  $C_0$  was the initial concentration of reactant;  $C_r$  and  $C_p$  were the concentrations of reactant and target product, respectively, at a certain time after the photocatalytic reaction. To further evaluate the stability of the as-synthesized samples, the sample was recycled and reused five times in the photocatalytic selective oxidation of aromatic alcohols and reduction of nitrobenzene under the same conditions. After each photocatalytic reaction, the solution was centrifuged to recycle the sample powders which were then dried at 60 °C for another test. Though the sample was stable and not dissolved in the photocatalytic reaction under visible light irradiation, loss of sample was inevitable in the recycling process. Therefore, a small amount of fresh sample was added to maintain the initial weight of 0.1 g for each test.

### 3. Results and discussion

#### 3.1. Characterization of photocatalysts

The crystal structure properties and phase compositions of the samples were investigated by XRD analysis. As shown in Fig. 1a, CdS-G and CdS-P exhibit similar XRD patterns. The peaks of scattering angles ( $2\theta$  values) located at *ca.* 26.5°, 43.9°, and 52.1° are attributed to the diffraction of the (111), (220), and (311) crystal planes of cubic CdS (JCPDS no. 10-0454), respectively.<sup>27</sup> Moreover, the diffraction peaks are broad. This may be caused by the relatively small crystallite sizes of the CdS-G and CdS-P samples. On the basis of the Scherrer formula,<sup>28</sup> the average crystallite sizes of CdS-G and CdS-P samples are about 11.6 and 7.2 nm, respectively. However, CdS-H sample prepared by the high-temperature hydrothermal method has a different phase by comparison with CdS-G and CdS-P. The peaks at  $2\theta$  values of 24.8, 26.5, 28.2, 36.6, 43.7, 47.9, 50.9, 51.8, 52.8, 66.8, 69.2, 70.9, 72.3, and 75.4° are distinctly indexed to the (100), (002), (101), (102), (110), (103), (200), (112), (201), (203), (210), (211), (114), and (105) crystal planes, respectively, of CdS with a hexagonal phase (JCPDS no. 41-1049).<sup>10</sup> Furthermore, no impurity peaks were detected in all of the CdS samples, revealing the high purity of the as-synthesized products. From the results obtained, it can be concluded that cubic-phase CdS is readily prepared by solid-state reaction at room temperature. In contrast, high temperature contributes to formation of the hexagonal phase CdS crystal structure.

To further investigate the surface element composition and the chemical status of the as-synthesized CdS-G, XPS analysis was carried out. Fig. 1b displays the survey XPS spectrum, which shows that no peaks from other elements apart from Cd, S, C, and O are observed. The carbon and oxygen peaks are attributed to the graphite conductive adhesive or the absorbed gaseous molecules. Fig. 1c and d present the high-resolution spectra of the Cd 3d and S 2p regions, respectively. The binding energies corresponding to Cd 3d<sub>5/2</sub> and Cd 3d<sub>3/2</sub> are 404.7 and 411.5 eV, respectively, indicative of Cd<sup>2+</sup> in CdS. The 6.8 eV difference between the binding energies of Cd 3d<sub>5/2</sub> and Cd 3d<sub>3/2</sub> peaks is also characteristic of Cd<sup>2+</sup> states.<sup>29,30</sup> In addition, as shown in Fig. 1d, the binding energies of S 2p for S 2p<sub>3/2</sub> and S 2p<sub>1/2</sub> were determined to be about 161.4 and 162.5 eV, respectively, demonstrating a normal state of S<sup>2-</sup> in the CdS-G sample.<sup>31,32</sup> Hence, XPS results undoubtedly confirm successful synthesis of cubic CdS *via* a facile solid-state reaction at room temperature and are in agreement with the XRD results.

SEM and TEM analysis were performed to investigate the morphology. As shown in Fig. 2a and d, it is clear that CdS-G consisted of small nanoparticles (the grain size is about 10–20 nm, which agrees well with the XRD result) with some degree of agglomeration. The lattice fringe can be clearly seen in the HR-TEM image (Fig. 2g), indicating that the CdS-G nanoparticles possess good crystallization. The spacing is 0.336 nm, which can be indexed to the [111] crystal face of the cubic CdS phase. Meanwhile, the other cubic phase, CdS-P,

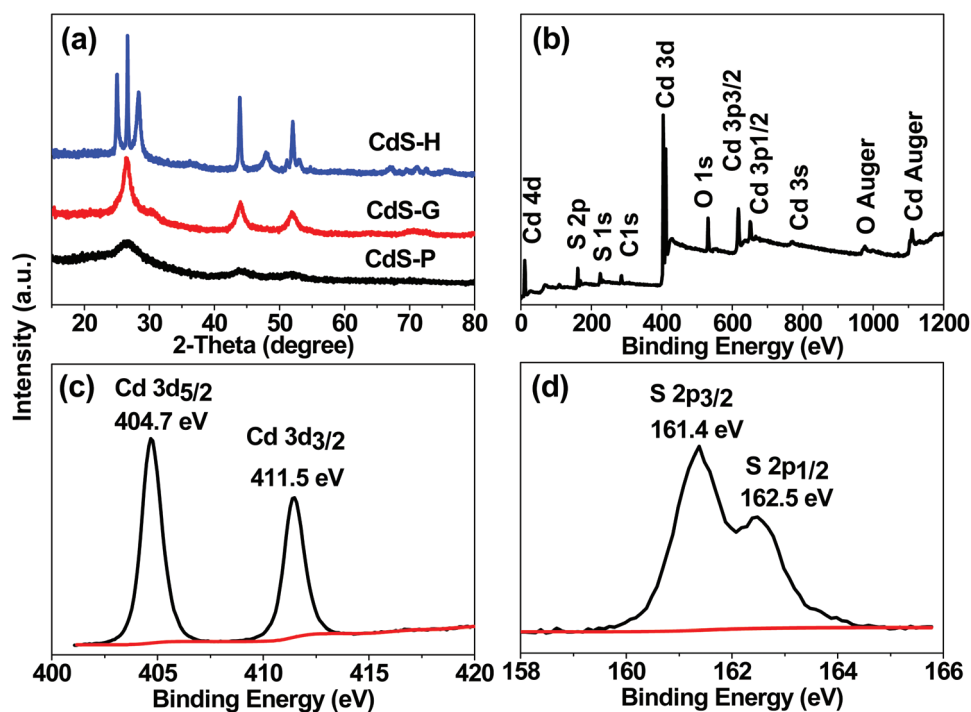


**Fig. 1** (a) The XRD patterns of the CdS samples synthesized by different methods. (b) XPS survey spectrum and high-resolution spectra of (c) Cd 3d, (d) S 2p of CdS-G.

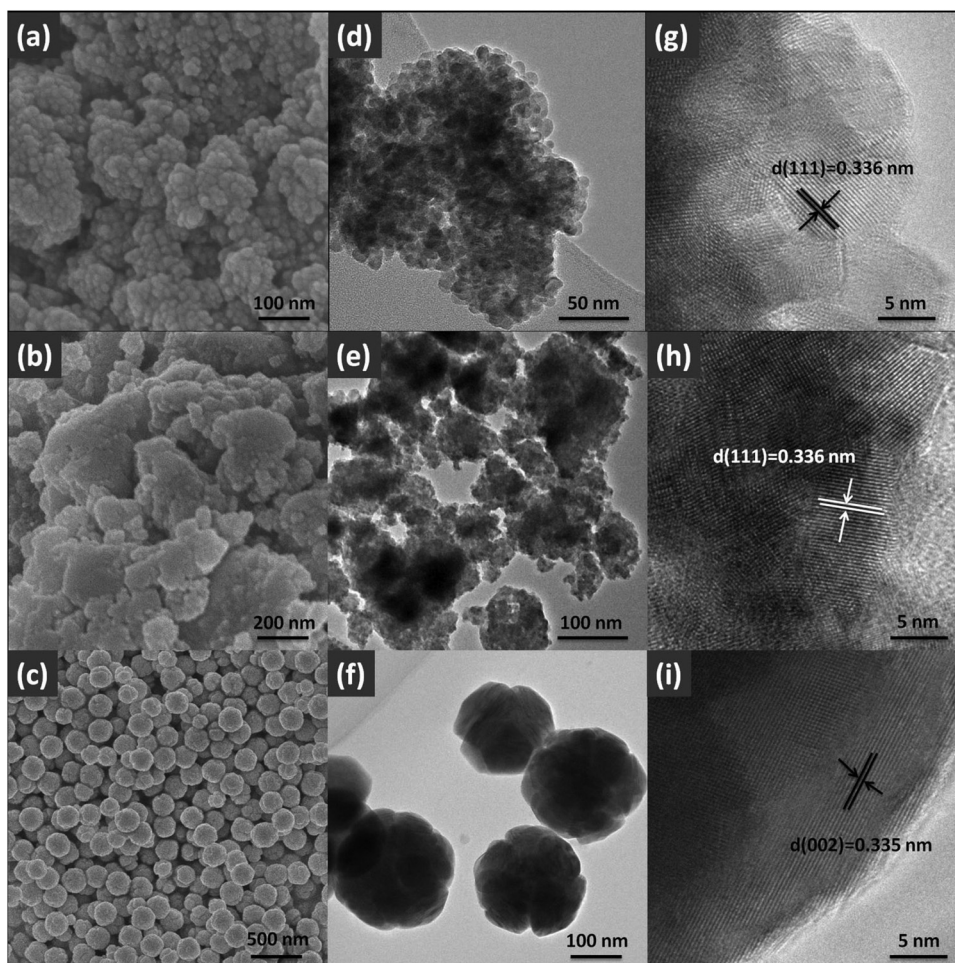


**Fig. 2** Typical SEM (a, b, c), TEM (d, e, f) and HR-TEM (g, h, i) images of the as-prepared CdS samples: CdS-G (a, d, g), CdS-P (b, e, h) and CdS-H (c, f, i).

synthesized by the precipitation method, is comprised of block-based flakiness and is of irregular shape (Fig. 2b). This typical feature sheet structure resulting from the accumulation of small nanoparticles can be clearly observed by detailed TEM analysis<sup>27</sup> (Fig. 2e). Moreover, the HR-TEM image in Fig. 2h also indicates that the sheet structured CdS-P consisted of small cubic CdS crystallites with particle size of less than 10 nm. From Fig. 2c and f, it can be seen that the sample CdS-H exhibits uniform nanospheres, and the average diameter of the as-prepared CdS-H nanospheres is around 200 nm. Furthermore, the clear lattice spacing (about 0.335 nm between adjacent lattice planes of the CdS-H sample in Fig. 2i) is consistent with the *d*-spacing of the hexagonal CdS [002] plane. This is in accordance with a previous report.<sup>10</sup>

UV-Vis DRS are widely used to measure the optical properties of the semiconductor powder materials. Fig. 3 displays a comparison of the UV-Vis DRS of the CdS samples. It can be seen that all of the CdS samples demonstrate high photo-absorption capacity in visible light around 520 nm, suggesting their potential photocatalytic activity under visible light. A plot obtained *via* the transformation based on the Kubelka-Munk

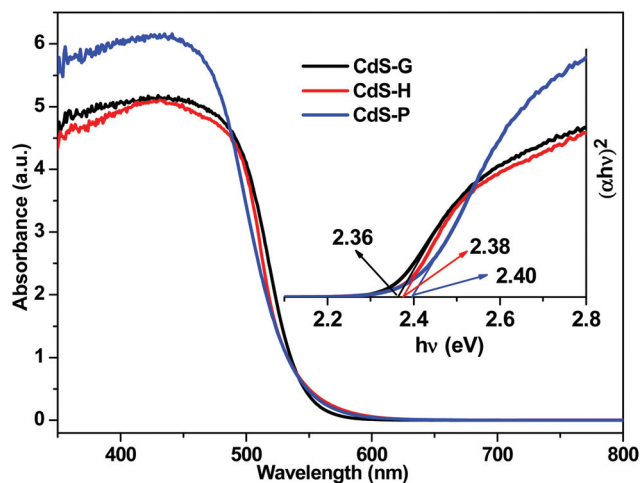


**Fig. 3** UV-Vis diffuse reflectance spectra (DRS) and band gap energies (inset) of the CdS samples.

function<sup>33,34</sup> versus the energy of light is shown in the inset of Fig. 3. The estimated band-gap values of the samples are approximately 2.36, 2.40 and 2.38 eV, corresponding to CdS-G, CdS-P and CdS-H, respectively. The difference in band gap could possibly be caused by different crystal phases (CdS-G and CdS-P are cubic phase, CdS-H is hexagonal phase), or crystal size (the particle sizes of CdS-G, CdS-P and CdS-H are about 10–20, <10 and 200 nm, respectively). Generally, for the same phase, the particle size, the band gap, and morphology (the morphologies of CdS-G, CdS-P and CdS-H are nanoparticle, block-based flakiness, and nanosphere, respectively) would lead to a different degree of delocalization and mobility of photoexcited electron–hole pairs, hence would have different photocatalytic efficiencies. Moreover, the narrow band gap of the CdS-G sample suggests that it would most easily absorb more visible light and be photoexcited to generate more electron–hole pairs by visible light irradiation, consequently contributing to triggering chemical redox reactions.<sup>27</sup>

In order to examine the specific surface area ( $S_{\text{BET}}$ ) and pore-size distribution of the catalysts, BET (Brunauer–Emmett–Teller) gas-sorption measurements were carried out at 77 K. Fig. 4 shows the  $\text{N}_2$  adsorption/desorption isotherms for the three CdS samples. Based on the BDDT (Brunauer–Deming–Deming–Teller) classification, the isotherm of CdS-G is identified as type IV, which is characteristic of mesoporous materials.<sup>35</sup> In addition, the isotherm with a broad hysteresis loops at relative pressure ( $P/P_0$ ) between 0.4 and 1.0 corresponded to an H2 hysteresis loop associated with ink-bottle pores. The  $S_{\text{BET}}$  of CdS-G is as much as  $39 \text{ m}^2 \text{ g}^{-1}$ . The corresponding pore-size distribution curve (inset in Fig. 4) of the CdS-G sample exhibits a relatively wide pore-size distribution from 2 to 10 nm, which will provide efficient transport pathways for reactant and product molecules.<sup>31</sup> However, the isotherm of the CdS-P sample is slightly different

from CdS-G. From the isotherm, it is clear that CdS-P has two hysteresis loops, indicating bimodal pore-size distributions. At low relative pressures between 0.4 and 0.8, the hysteresis loops are of type H2, which corresponds to ink-bottle pores. The shape of the hysteresis loop is of type H3 at high relative pressures between 0.8 and 1.0.<sup>36</sup>  $S_{\text{BET}}$  of CdS-P is  $32 \text{ m}^2 \text{ g}^{-1}$ , and the pore-size distribution is about 2–5 nm. Further observations from Fig. 4 show that the hysteresis loop of CdS-G is larger compared with the CdS-H and CdS-P samples, indicating that CdS-G has the largest pore volume. The pore volumes of CdS-G and CdS-P were demonstrated to be about  $0.128$  and  $0.082 \text{ cm}^3 \text{ g}^{-1}$ , respectively. Because CdS-H is comprised of large solid spheres, the pore structure is undetectable and  $S_{\text{BET}}$  of CdS-H is very low ( $5 \text{ m}^2 \text{ g}^{-1}$ ). In general, a photocatalyst with a high specific surface area and a large pore volume is indispensable for improving photocatalytic performance. This is mainly due to the combined effects of many factors, such as more surface active sites, ease of transportation of reactant molecules, and enhanced harvesting of irradiation light by multiple scattering.<sup>37</sup>

Based on the results, clearly the nanoparticle structured CdS-G sample has been readily prepared *via* a facile solid-state reaction at room temperature, and it is reasonable to speculate that CdS-G is a promising photocatalyst in view of its excellent visible-light absorption, larger BET surface area, pore-size distribution and pore volume.

### 3.2. Photocatalytic performance of the CdS samples

The photocatalytic performance of the CdS samples was estimated by selective oxidation of pMBA to pMBAD and reduction of NB to AL in one reaction system (inert  $\text{N}_2$  atmosphere) under visible-light irradiation ( $\lambda > 420 \text{ nm}$ ). To further probe the details of activity and selectivity distribution of product for oxidation of pMBA and reduction of NB, we have performed the time-online reaction profile with irradiation time. As displayed in Fig. 5, the conversions of pMBA and NB and the yields of pMBAD and AL all increased gradually with irradiation time. When the irradiation time was 30 min, the conversions of pMBA and NB reached 46.0% and 52.7%, respectively. After irradiation for 4 h, the conversions of pMBA and NB reached up to 92.2% and 93.3% with high yields of pMBAD (83.5%) and AL (62.3%), respectively. Negligible photoactivities were observed in the blank experiments (without catalyst or light irradiation), which confirmed that the redox reactions are truly driven by a photocatalytic process.

To determine the optimal amount of catalyst, a succession of experiments was also performed. As shown in Fig. 6, as far as yield and selectivity were concerned, when the amount of catalyst was 0.1 g, it exhibited the highest photocatalytic activity (yields (selectivities) of pMBAD and AL were about 83.5% (90.6%) and 62.3% (66.8%), respectively). However, when the amount of CdS photocatalyst exceeded 0.1 g, the yields and selectivities of pMBAD and AL both decreased. This may be the reason why the amount of photocatalyst added can produce a difference in light transmittance. A large number of

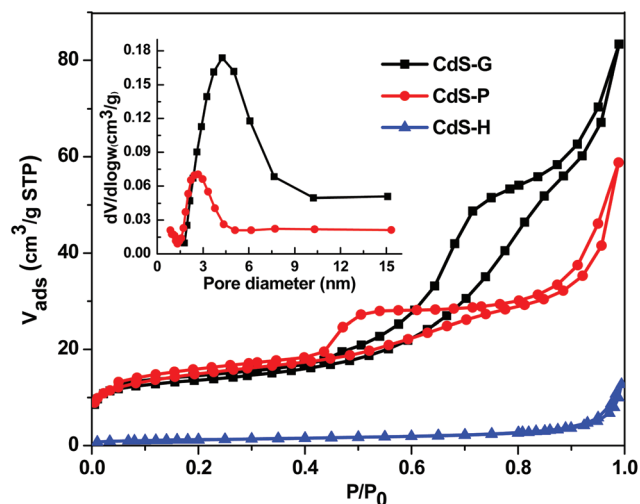


Fig. 4 Nitrogen adsorption–desorption isotherms and the corresponding pore-size distribution curves (inset) of the CdS samples.

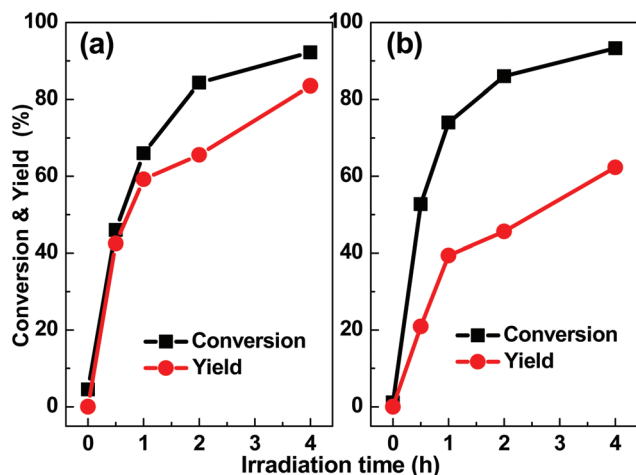


Fig. 5 Time-online photocatalytic selective (a) oxidation of pMBA to pMBAD and (b) reduction of NB to AL over CdS-G under visible-light irradiation.

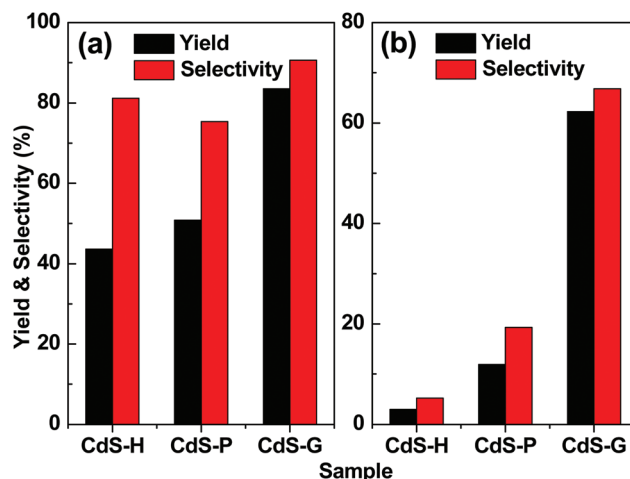


Fig. 7 Activity of CdS-H, CdS-P, and CdS-G for photocatalytic selective (a) oxidation of pMBA to pMBAD and (b) reduction of NB to AL under visible-light irradiation.

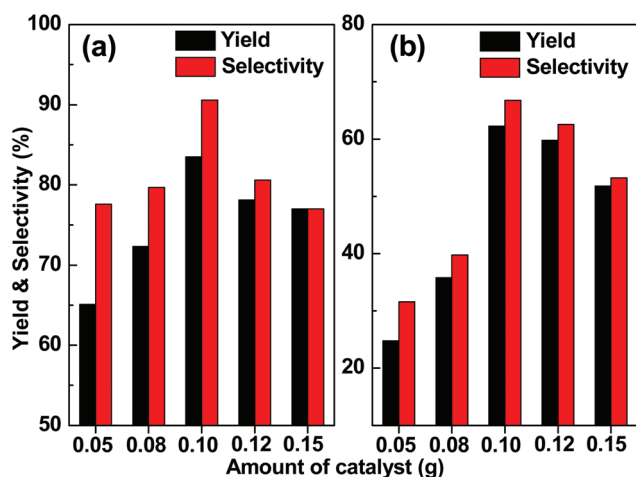


Fig. 6 Photocatalytic activity with different amounts of CdS-G catalyst for photocatalytic selective (a) oxidation of pMBA to pMBAD and (b) reduction of NB to AL under visible-light irradiation.

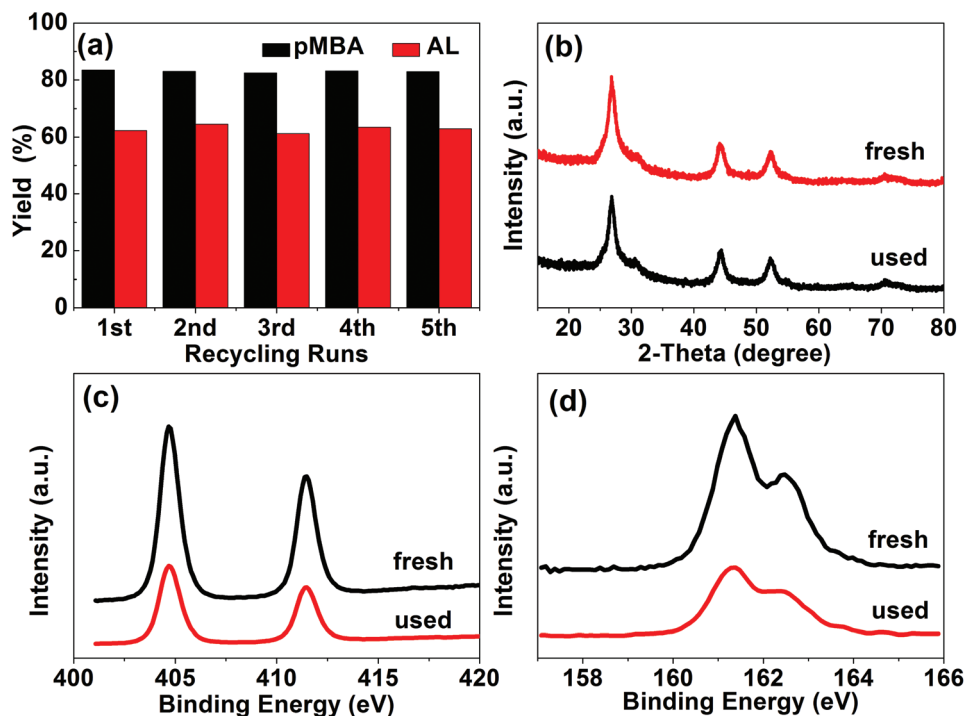
submerged catalysts cannot be irradiated by light, and the photocatalytic reaction may only occur on the surface suspended catalyst. This is normal in a liquid-phase photocatalyst. On the basis of the results, 0.1 g and 4 h were chosen as the optimal amount of CdS photocatalyst and illumination time, respectively.

Fig. 7 shows the results of photocatalytic selective oxidation of pMBA to pMBAD and reduction of NB to AL over CdS-H, CdS-P and CdS-G in one reaction system under visible light irradiation. It was found that all of the as-synthesized CdS photocatalysts display activity toward the oxidation of pMBA to pMBAD and reduction of NB to AL under mild conditions. Among the as-prepared CdS samples, CdS-G exhibits the best photocatalytic performance. Moreover, the photoactivity of

CdS-G is also higher than the optimum CdS/g-C<sub>3</sub>N<sub>4</sub> photocatalyst (yield of pMBAD (AL) is 52.3% (40%)) as reported recently<sup>26</sup> (under identical reaction conditions).

To further confirm the high photoactivity of the CdS-G sample, we have also conducted activity testing on oxidation of other aromatic alcohols and reduction of other nitro-aromatic compounds under the same conditions. As demonstrated in Fig. S1,<sup>†</sup> the CdS-G photocatalyst also exhibits high photocatalytic activity in selective oxidation/reduction of benzyl alcohol/nitrobenzene and benzyl alcohol/*p*-chloronitrobenzene in a synergetic reaction system. Hence, clearly the idea of selective oxidation of aromatic alcohols and reduction of nitro-aromatic organics in a coupled reaction system under visible light irradiation is confirmed, and the as-prepared CdS-G shows excellent photocatalytic activity.

As is known, in addition to high activity, reusability is another significant characteristic of a catalyst. To evaluate CdS-G for practical applications, the photostability and reusability of the as-prepared CdS-G for photocatalytic selective oxidation of pMBA and reduction of NB in one reaction system have also been investigated. First, CdS-G was reused five times and the reaction conditions were kept identical. As shown in Fig. 8a, the photocatalyst CdS-G exhibited satisfactory stability in the recycled testing, which showed almost no deactivation. To learn whether there was a change in the bulk and surface composition after the photocatalytic selective reactions, XRD and XPS techniques were further carried out to characterize the fresh and used CdS-G. As displayed in Fig. 8b, the used CdS-G had identical XRD patterns compared to the fresh CdS-G, which indicated that no significant change occurred in the bulk phase composition. The contrast XPS results of typical Cd 3d and S 2p spectra (Fig. 8c and d) further indicated that the used CdS-G had a similar surface composition to that of the fresh CdS-G. In addition, the amount of Cd<sup>2+</sup> in the reaction supernatant liquid was analyzed by inductively



**Fig. 8** (a) Recycled testing of photocatalytic activity of CdS-G toward the selective oxidation of pMBA to pMBAD and reduction of NB to AL under visible-light irradiation for 4 h. Contrast (b) XRD spectra, XPS high-resolution spectra of (c) Cd 3d and (d) S 2p of fresh CdS-G and used CdS-G samples after visible light irradiation.

coupled plasma-mass spectrometry (ICP-MS). The result showed that the amount of  $\text{Cd}^{2+}$  was only 6.3 ppb. Therefore, it is concluded that the as-prepared CdS-G semiconductor is a stable visible-light-driven photocatalyst for the selective oxidation of pMBA and reduction of NB in a coupled reaction system under mild conditions.

### 3.3. Origins of the higher photocatalytic performance of CdS-G

To understand and explore the origins of the higher photocatalytic performance of CdS-G for selective oxidation of pMBA and reduction of NB than that of CdS-P or CdS-H, a series of characterizations have been carried out. The results of the transient photocurrent response of CdS-G, CdS-P and CdS-H electrodes under visible light irradiation are shown in Fig. 9a, which illustrates that the photocurrent density of CdS-G under visible light illumination is much higher than that of the other CdS samples. It is known that the photocurrent is generated mainly by collection of the diffusion of photoinduced electrons to the back contact, and at the same time, the photo-generated holes are taken up by the hole acceptors in the electrolyte.<sup>38</sup> Hence, the higher photocurrent over CdS-G implies not only high yield of photoinduced electron-hole pairs, but also longer lifetime of the photogenerated charge carriers compared with the other two CdS samples. In addition, it is well worth noting that there is obvious photocurrent decay during the initial runs of photocurrent transient response for CdS-G, demonstrating the competitive process of

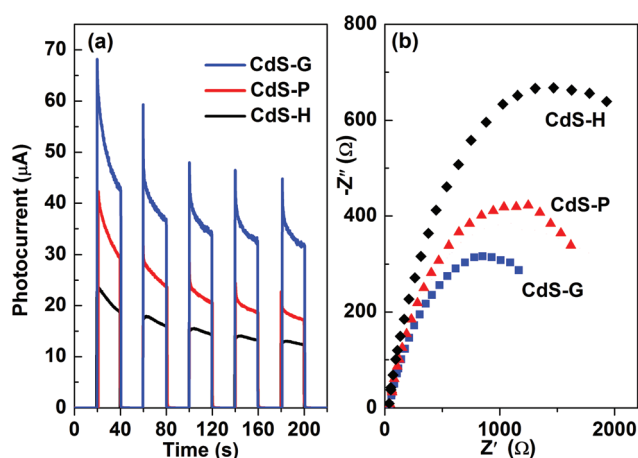


**Fig. 9** (a) Photocurrent transient response of the samples in a 0.1 M  $\text{Na}_2\text{SO}_4$  aqueous solution without bias versus Ag/AgCl electrode under visible light irradiation. (b) Nyquist impedance plots of the samples in 0.1 M KCl aqueous solution containing 0.01 M  $\text{K}_3[\text{Fe}(\text{CN})_6] - \text{K}_4[\text{Fe}(\text{CN})_6]$ .

charge carrier recombination and separation.<sup>39</sup> Nevertheless, when the competitive process reaches equilibrium, the photocurrent will reach a relatively constant value, as shown in the last three runs in Fig. 9a.

In previous studies, the diameters of the EIS plots are thought to show the charge separation and transfer resistance across the solid-liquid junction in the electrode-electrolyte interface region.<sup>40</sup> Therefore, electrochemical impedance spec-

troscopy (EIS) has been performed to study the migration of charge carriers in the electrode materials.<sup>41</sup> Fig. 9b shows the EIS Nyquist plots of the CdS electrode materials cycled in 0.1 M KCl aqueous solution containing 0.1 M  $K_3[Fe(CN)_6]$ - $K_4[Fe(CN)_6]$  (1:1). It is clearly seen that the three-electrode materials all show semi-cycles at high frequencies. Under similar preparation of the electrodes and electrolyte, the high-frequency arc corresponded to the charge transfer limiting process and it may be attributed to the charge transfer resistance at the contact interface between the electrode and electrolyte solution.<sup>10</sup> The smallest arc radius of the EIS Nyquist plot of CdS-G exhibits the fastest interfacial electron transfer compared with CdS-P and CdS-H.<sup>42,43</sup>

In addition, the inhibition of photogenerated electron-hole pair recombination over CdS samples has been further verified by photoluminescence (PL) analysis.<sup>44</sup> Generally, a lower PL intensity demonstrates a lower recombination rate of photogenerated charge carriers. As shown in Fig. 10, it is clear that CdS-G exhibits the weakest PL intensity (CdS-G < CdS-P < CdS-H), suggesting that the recombination rate of the photogenerated electron-holes on CdS-G is efficiently restrained. This is in accordance with the photoelectrochemical result and also consistent with the examination of photocatalytic activity. Moreover, it should be stressed that, as CdS-G coupled with BTF and reactants, the PL intensity of CdS-G could be significantly quenched, suggesting that the recombination of photogenerated electron-holes over CdS in BTF solvent with reactants is mostly inhibited. The PL intensity gap between CdS-G + BTF + reactants and CdS-G + BTF implies that the photogenerated electron-holes might be trapped by the reactants. In other words, the photogenerated electron-holes were efficiently utilized by the reactants, which led to corresponding photocatalytic redox actions in one reaction system with high photocatalytic performance.

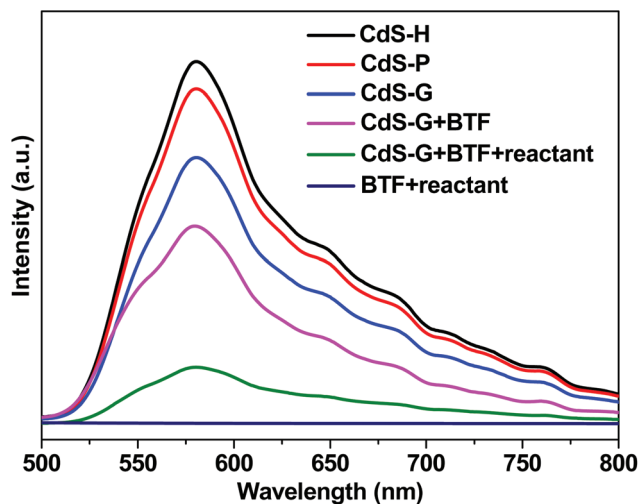


Fig. 10 Photoluminescence (PL) spectra of the as-synthesized samples with an excitation wavelength of 440 nm.

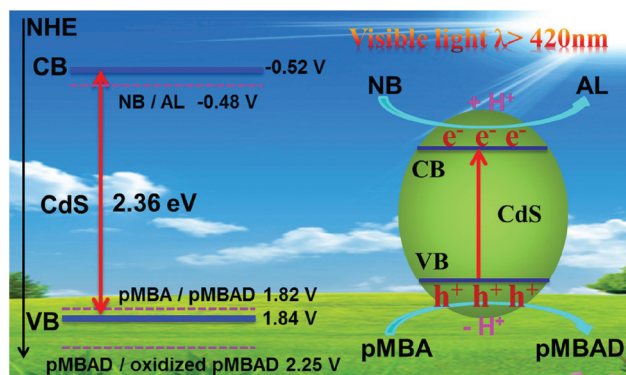


Fig. 11 Band positions of CdS-G and redox potentials of pMBA, pMBAD and NB; and the proposed photocatalysis mechanism for selective oxidation of pMBA and reduction of NB over CdS-G under visible light irradiation.

In order to verify the feasibility of the photocatalytic redox action in a synergetic system by CdS catalyst, the redox potentials of pMBA, pMBAD and NB at different concentrations (0.1, 0.2, and 0.5 mmol L<sup>-1</sup>) were measured by cyclic voltammetry.<sup>6,7,45</sup> Fig. S2† shows that the redox potentials of pMBA, pMBAD and NB are independent of concentration. The voltammogram of pMBA exhibits an irreversible curve and possesses two oxidative potentials (Fig. S2a†): the first oxidative potential (*ca.* +1.62 V vs. Ag/AgCl) is assigned to pMBA/pMBAD; the second oxidative potential (*ca.* +2.05 V vs. Ag/AgCl) belongs to pMBAD/acid, which can be clearly seen in Fig. S2b.† Similarly, the cyclic voltammogram of NB has been recorded in Fig. S2c.† The reductive potential of NB is -0.68 V vs. Ag/AgCl. Moreover, the band position of the as-prepared CdS-G photocatalyst was evaluated by Mott-Schottky plot (Fig. S2d†). It was found that the slope of the linear  $1/C^2$  potential curve was positive, indicating that CdS has an n-type semiconductor characteristic.<sup>46,47</sup> The flat-band potential ( $V_{fb}$ ) of CdS-G was determined from extrapolation to the X intercept in the Mott-Schottky plot at various frequencies.  $V_{fb}$  of CdS is approximately -0.72 V vs. Ag/AgCl. Therefore, the conduction band (CB) and valence band (VB) positions are -0.52 V and 1.84 V, respectively. Fig. 11 presents the positions of the conduction band and valence band of CdS-G and the redox potentials of NB, pMBA/pMBAD and pMBAD/oxidized pMBAD, which reveal that the conduction band of CdS-G is more negative than the reductive potential of NB, and the valence band of CdS-G is more positive than the oxidative potential of pMBA/pMBAD, but is not more positive than pMBAD/oxidized pMBAD. Therefore, a green photocatalytic process for selective oxidation of pMBA to pMBAD (the photogenerated holes cannot further oxidize pMBAD) and reduction of NB to AL can be achieved using CdS-G photocatalyst in a coupled system under visible light illumination with high selectivity.

### 3.4. Reaction mechanism

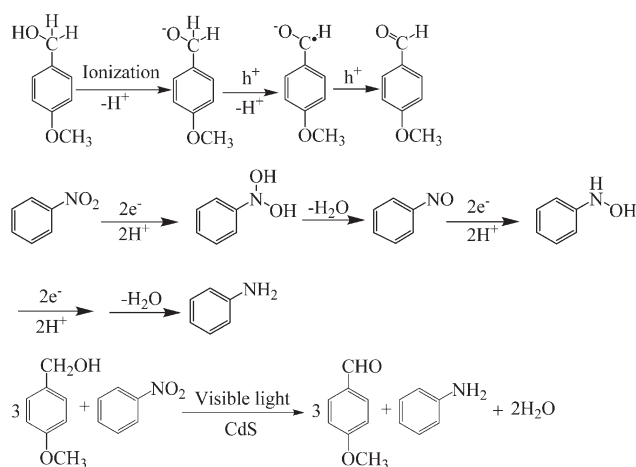
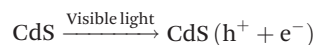
In order to investigate the possible mechanism for selective oxidation of pMBA and selective reduction of NB in a coupled

system over CdS, a series of controlled experiments were carried out. In the study, *tert*-butyl alcohol (TBA), tetrachloromethane (CCl<sub>4</sub>) and triethanolamine (TEA) were used as scavengers for trapping ·OH radical species, photogenerated electrons, and holes, respectively.<sup>6,48</sup> As shown in Fig. 12, when CCl<sub>4</sub> was added to the reaction system, the yield of AL decreased significantly, implying that the photogenerated electrons are the major reductive species for the selective reduction of NB to AL. At the same time, the yield of pMBAD increased, suggesting that trapping of photogenerated electrons with CCl<sub>4</sub> could benefit the photogenerated holes inducing selective oxidation of pMBA to pMBAD under visible light, which is in accordance with the previous report about selective oxidation of benzyl alcohol over Bi<sub>12</sub>O<sub>17</sub>Cl<sub>2</sub>.<sup>6</sup> The ·OH trapping experiment was also performed. The results indicated that the activity of selective oxidation of pMBA to pMBAD remains virtually constant. This implies that ·OH radical species does not play an important role in oxidation of pMBA. While the activity of reduction of NB to AL is improved, this may be because the additional TBA could provide protons. The result is in agreement with the addition of phenol or excess pMBA.

When TEA was added to the reaction system, the yield of pMBAD clearly decreased, indicating that the photogenerated holes play a significant role in oxidation of pMBA. While the addition of hole scavenger TEA did not improve the yield of AL, and when pMBA was not added to the reaction system, no conversion of NB was observed. This suggests that the reduction of NB could be blocked by the shutdown of oxidation of pMBA. This may be because protons are produced in the oxidation of pMBA and are necessary for reduction of NB to AL. These protons and photogenerated electrons dominated the fate of the action of reduction NB to AL. In this one coupled reaction system, photocatalytic reduction of NB was triggered after oxidation of pMBA. Furthermore, in the system without the addition of NB, the yield of pMBAD (46.6%)

decreased. This might be because the existence of NB can quench the electrons which contributed to inhibiting the combination of the photogenerated carriers and separating the photogenerated electron-hole pairs efficiently. Therefore, pMBA and NB are synergetic and mutual promoters in the coupled system.

On the basis of the above results and previous reports, a possible pathway for the photocatalytic selective oxidation of aromatic alcohols and reduction of nitrobenzene over CdS photocatalyst under visible light was proposed, as follows:



First, CdS nanoparticles are excited under visible light and form photogenerated electrons–holes. pMBA is deprotonated to form alkoxide anions, and then the alkoxide anions would react with the photogenerated holes, and subsequently deprotonate to form carbon radicals. The carbon radicals further react with the photogenerated holes to form aromatic aldehyde. Two protons are generated and two holes are consumed in the process of selective oxidation of pMBA to pMBAD. At the same time, the photogenerated electrons and protons released from oxidation of pMBA are quenched by NB. NB loses water molecules and generates the intermediate product nitrosobenzene, which was detected in the reaction (the spectra of GC in Fig. S3†). With the increase in light exposure time, nitrosobenzene was gradually transformed into the final product aniline. In this reduction process, six electrons and six protons are required, and two water molecules are produced. Therefore, according to theoretical analysis, the amount of pMBAD should be three times that of AL. In fact, the generated amount of AL is lower than the theoretical value (Fig. 12). This may be because of the lag effect in the system. The generated amount of H<sup>+</sup> is not fully used by NB. However, if the amount of pMBA is four times that of NB, the yield of AL can be enhanced by the additional amount of H<sup>+</sup> (Fig. 12). Moreover, the yield of AL can also be improved by addition of phenol to the reaction system to provide H<sup>+</sup> (Fig. 12). Hence, the ratio of pMBAD and AL can approximately achieve the theoretical value. It should be noted that the amount of pMBA is three

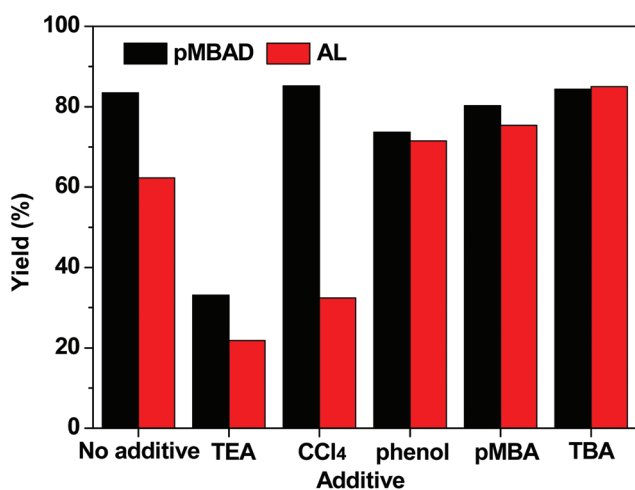


Fig. 12 Yield of pMBAD and AL over CdS-G with different additives under visible light for 4 h.

times that of NB in the reaction system. Therefore, the yield of pMBAD is equal to that of AL.

## 4. Conclusion

A cubic phase CdS semiconductor has been synthesized by a facile solid-state reaction at room temperature for the first time. Compared with CdS obtained by the precipitate method and CdS prepared by hydrothermal treatment, the CdS-G photocatalyst exhibits excellent photocatalytic activity toward the selective oxidation of aromatic alcohols to aromatic aldehydes and reduction of nitro-organics to corresponding aniline in one reaction system under visible light irradiation. The highly selective photoactivity is attributed to its well matched conduction band and valence band positions, large surface area and pore volume, efficient visible light absorption and highly effective separation of photogenerated charge carriers. The as-synthesized CdS-G also shows excellent photostability and reusability because the photogenerated holes and electrons can be efficiently and directly reacted with pMBA and NB, respectively. The yield of pMBAD and AL can be successfully achieved at a theoretical ratio of 1 : 1. The results of this work are of great value in practice and useful in the utilization of clean and safe solar energy. We hope that this work will expand the highly efficient visible-light-driven photocatalysts available for selective oxidation of aromatic alcohols to aromatic aldehydes and reduction of nitro-organics to corresponding aniline in a coupled system using solar light as an energy source under mild conditions.

## Acknowledgements

This work was financially supported by the Natural Science Foundation of China (NSFC, grant no. 51472005, 51172086, 51272081, 21473066, 21103060 and 21203029), the Natural Science Foundation of Anhui Province (grant no. 1408085QB38 and 1608085QB37), the High Education Revitalization Plan of Anhui province, and the Foundations of Natural Science of Anhui Education Committee (KJ2014A230).

## References

- 1 K. K. Sakimoto, A. B. Wong and P. Yang, *Science*, 2016, **351**, 74–77.
- 2 (a) N. Zhang, R. Ciriminna, M. Pagliaro and Y.-J. Xu, *Chem. Soc. Rev.*, 2014, **43**, 5276–5287; (b) F.-X. Xiao, Z. Zeng and B. Liu, *J. Am. Chem. Soc.*, 2015, **137**, 10735–10744; (c) F.-X. Xiao, J. Miao and B. Liu, *J. Am. Chem. Soc.*, 2014, **136**, 1559–1569; (d) F.-X. Xiao, Z. Zeng, S.-H. Hsu, S.-F. Hung, H. M. Chen and B. Liu, *ACS Appl. Mater. Interfaces*, 2015, **7**, 28105–28109; (e) F.-X. Xiao, J. Miao, H.-Y. Wang, H. Yang, J. Chen and B. Liu, *Nanoscale*, 2014, **6**, 6727–6737; (f) F.-X. Xiao, J. Miao, H.-Y. Wang and B. Liu, *J. Mater. Chem. A*, 2013, **1**, 12229–12238.
- 3 (a) Y. Zheng, L. Lin, B. Wang and X. Wang, *Angew. Chem., Int. Ed.*, 2015, **54**, 12868–12884; (b) J. Yuan, J. Wen, Y. Zhong, X. Li, Y. Fang, S. Zhang and W. Liu, *J. Mater. Chem. A*, 2015, **3**, 18244–18255; (c) J.-J. Zhou, R. Wang, X.-L. Liu, F.-M. Peng, C.-H. Li, F. Teng and Y.-P. Yuan, *Appl. Surf. Sci.*, 2015, **346**, 278–283; (d) Q. Wang, J. Li, Y. Bai, J. Lian, H. Huang, Z. Li, Z. Lei and W. Shangguan, *Green Chem.*, 2014, **16**, 2728–2735.
- 4 C. K. Prier, D. A. Rankic and D. W. C. MacMillan, *Chem. Rev.*, 2013, **113**, 5322–5363.
- 5 F. Su, C. S. Mathew, G. Lipner, X. Fu, M. Antonietti, S. Blechert and X. Wang, *J. Am. Chem. Soc.*, 2010, **132**, 16299–16301.
- 6 X. Xiao, J. Jiang and L. Zhang, *Appl. Catal., B*, 2013, **142**, 487–493.
- 7 (a) S. Higashimoto, N. Suetsugu, M. Azuma, H. Ohue and Y. Sakata, *J. Catal.*, 2010, **274**, 76–83; (b) S. Higashimoto, K. Okada, M. Azuma, H. Ohue, T. Terai and Y. Sakata, *RSC Adv.*, 2012, **2**, 669–676.
- 8 (a) N. Zhang, M.-Q. Yang, Z.-R. Tang and Y.-J. Xu, *ACS Nano*, 2014, **8**, 623–633; (b) N. Zhang, M.-Q. Yang, Z.-R. Tang and Y.-J. Xu, *J. Catal.*, 2013, **303**, 60–69.
- 9 S. Földner, P. Pohla, H. Bartling, S. Dankesreiter, R. Stadler, M. Gruber, A. Pfitzner and B. König, *Green Chem.*, 2011, **13**, 640–643.
- 10 Z. Chen, S. Liu, M. Yang and Y. Xu, *ACS Appl. Mater. Interfaces*, 2013, **5**, 4309–4319.
- 11 C. Han, Z. Chen, N. Zhang, J. Colmenares and Y.-J. Xu, *Adv. Funct. Mater.*, 2015, **25**, 221–229.
- 12 (a) A. Baiker and T. Mallat, *Chem. Rev.*, 2004, **104**, 3037–3058; (b) E. A. Gelder, S. D. Jackson and C. M. Lok, *Chem. Commun.*, 2005, **4**, 522–524.
- 13 (a) M. Zhang, Q. Wang, C. Chen, L. Zang, W. Ma and J. Zhao, *Angew. Chem., Int. Ed.*, 2009, **121**, 6197–6200; (b) S. Patel and B. K. Mishra, *J. Org. Chem.*, 2006, **71**, 6759–6766.
- 14 (a) S. Diao, W. Qian, G. Luo, F. Wei and Y. Wang, *Appl. Catal., A*, 2005, **286**, 30–35; (b) J. Wisniak and M. Klein, *Ind. Eng. Chem. Prod. Res. Dev.*, 1984, **23**, 44–50.
- 15 M. Zhang, C. Chen, W. Ma and J. Zhao, *Angew. Chem., Int. Ed.*, 2008, **120**, 9876–9879.
- 16 (a) M.-Q. Yang, N. Zhang, M. Pagliaro and Y.-J. Xu, *Chem. Soc. Rev.*, 2014, **43**, 8240–8254; (b) B. Weng and Y.-J. Xu, *ACS Appl. Mater. Interfaces*, 2015, **7**, 27948–27958; (c) L. Yuan, M.-Q. Yang and Y.-J. Xu, *Nanoscale*, 2014, **6**, 6335–6345; (d) C. Han, M.-Q. Yang, N. Zhang and Y.-J. Xu, *J. Mater. Chem. A*, 2014, **2**, 19156–19166.
- 17 C. Huang, W. Ye, Q. Liu and X. Qiu, *ACS Appl. Mater. Interfaces*, 2014, **6**, 14469–14476.
- 18 S. Meng, X. Ye, X. Ning, M. Xie, X. Fu and S. Chen, *Appl. Catal., B*, 2016, **182**, 356–368.
- 19 S. Sarina, S. Bai, Y. Huang, C. Chen, J. Jia, E. Jaatinen, G. A. Ayoko, Z. Bao and H. Zhu, *Green Chem.*, 2014, **16**, 331–341.
- 20 Z. Niu, D. Wang, R. Yu, Q. Peng and Y. Li, *Chem. Sci.*, 2012, **3**, 1925–1929.

- 21 (a) X. Chen, S. Shen, L. Guo and S. S. Mao, *Chem. Rev.*, 2010, **110**, 6503–6570; (b) J. Wen, X. Li, W. Liu, Y. Fang, J. Xie and Y. Xu, *Chin. J. Catal.*, 2015, **36**, 2049–2070; (c) S. Cao, J. Low, J. Yu and M. Jaroniec, *Adv. Mater.*, 2015, **27**, 2150–2176; (d) H. Yu, F. Chen, F. Chen and X. Wang, *Appl. Surf. Sci.*, 2015, **358**, 385–392; (e) H. Yu, X. Huang, P. Wang and J. Yu, *J. Phys. Chem. C*, 2016, **120**, 3722–3730.
- 22 S. Liu, M.-Q. Yang and Y.-J. Xu, *J. Mater. Chem. A*, 2014, **2**, 430–440.
- 23 M. R. Hoffmann, S. T. Martin, W. Choi and D. W. Bahnemann, *Chem. Rev.*, 1995, **95**, 69–96.
- 24 A.-Y. Zhang, L.-L. Long, C. Liu, W.-W. Li and H.-Q. Yu, *Green Chem.*, 2014, **16**, 2745–2753.
- 25 S. J. A. Moniz, S. A. Shevlin, D. J. Martin, Z.-X. Guo and J. Tang, *Energy Environ. Sci.*, 2015, **8**, 731–759.
- 26 X. Dai, M. Xie, S. Meng, X. Fu and S. Chen, *Appl. Catal., B*, 2014, **158**, 382–390.
- 27 Y. Zhang, N. Zhang, Z.-R. Tang and Y.-J. Xu, *Chem. Sci.*, 2012, **3**, 2812–2822.
- 28 Q. Li, B. Guo, J. Yu, J. Ran, B. Zhang, H. Yan and J. R. Gong, *J. Am. Chem. Soc.*, 2011, **133**, 10878–10884.
- 29 D. Wang, L. Wang and A. Xu, *Nanoscale*, 2012, **4**, 2046–2053.
- 30 H. Zhao, Y. Dong, P. Jiang, G. Wang, H. Miao, R. Wu, L. Kong, J. Zhang and C. Zhang, *ACS Sustainable Chem. Eng.*, 2015, **3**, 969–977.
- 31 W. Wang, J. Yu, Q. Xiang and B. Cheng, *Appl. Catal., B*, 2012, **119–120**, 109–116.
- 32 Q. Wang, J. Li, Y. Bai, J. Lian, H. Huang, Z. Li, Z. Lei and W. Shangguan, *Green Chem.*, 2014, **16**, 2728–2735.
- 33 S. Sakthivel and H. Kisch, *Angew. Chem., Int. Ed.*, 2003, **42**, 4908–4911.
- 34 M. A. Butler, *J. Appl. Phys.*, 1977, **48**, 1914–1920.
- 35 L. Nie, A. Meng, J. Yu and M. Jaroniec, *Sci. Rep.*, 2013, **3**, 3215.
- 36 L. Qi, J. Yu and M. Jaroniec, *Phys. Chem. Chem. Phys.*, 2011, **13**, 8915–8923.
- 37 (a) J. Yu, Y. Su and B. Cheng, *Adv. Funct. Mater.*, 2007, **17**, 1984–1990; (b) J. Yu, S. Liu and M. Zhou, *J. Phys. Chem. C*, 2008, **112**, 2050–2057.
- 38 S. Soedergren, A. Hagfeldt, J. Olsson and S.-E. Lindquist, *J. Phys. Chem.*, 1994, **98**, 5552–5556.
- 39 M.-Q. Yang, C. Han, N. Zhang and Y.-J. Xu, *Nanoscale*, 2015, **7**, 18062–18070.
- 40 Z. Hosseini, N. Taghavinia, N. Sharifi, M. Chavoshi and M. Rahman, *J. Phys. Chem. C*, 2008, **112**, 18686–18689.
- 41 D. Wang, D. Choi, J. Li, Z. Yang, Z. Nie, R. Kou, D. Hu, C. Wang, L. V. Saraf, J. Zhang, I. A. Aksay and J. Liu, *ACS Nano*, 2009, **3**, 907–914.
- 42 Y. Lv, Y. Liu, Y. Zhu and Y. Zhu, *J. Mater. Chem. A*, 2014, **2**, 1174–1182.
- 43 B. Qiu, M. Xing and J. Zhang, *J. Am. Chem. Soc.*, 2014, **136**, 5852–5855.
- 44 W. Tu, Y. Zhou, Q. Liu, Z. Tian, J. Gao, X. Chen, H. Zhang, J. Liu and Z. Zou, *Adv. Funct. Mater.*, 2012, **22**, 1215–1221.
- 45 S. Balasubramanian, *J. Lumin.*, 2004, **106**, 69–76.
- 46 D.-S. Kong, *Langmuir*, 2008, **24**, 5324–5331.
- 47 X. Yang, A. Wolcott, G. Wang, A. Sobo, R. C. Fitzmorris, F. Qian, J. Zhang and Y. Li, *Nano Lett.*, 2009, **9**, 2331–2336.
- 48 X. Wang, K. Maeda, A. Thomas, K. Takanabe, G. Xin, J. M. Carlsson, K. Domen and M. Antonietti, *Nat. Mater.*, 2009, **8**, 76–80.